Ion temperature effects on ion charge-state distributions of an electron cyclotron resonant ion source

D. R. Whaley
Department of Nuclear Engineering, University of Michigan, Ann Arbor, Michigan 48109

W. D. Getty
Department of Electrical Engineering and Computer Science, University of Michigan, Ann Arbor, Michigan 48109

(Received 7 June 1989; accepted 28 February 1990)

A method is described for determining ion cyclotron resonance (ICR) heating effects on multiply charged-ion energy distributions using a Monte Carlo fit to experimental time-of-flight spectrometer data. The method is general but is used here specifically to separate the effects of plasma ambipolar potential spread and ion temperature in an electron cyclotron resonance (ECR) heated magnetic mirror ion source (MIMI) [Phys. Fluids **28**, 3116 (1985)]. A steady-state equilibrium model is also developed that models the relevant atomic processes occurring in MIMI plasmas. This model and the Monte Carlo analysis are used to relate the effect of midplane ICR heating on end loss ion charge state distributions to its effect on the confined ion distributions. The model allows for collisional, moderately collisional, and collisionless confinement, specific to each charge state in the distribution. Both experiment and modeling show that increased ion temperature causes a shift to lower-Z ion populations in both the confined and end loss charge-state distributions.

I. INTRODUCTION

Recently, interest has developed in electron cyclotron resonance (ECR) heated minimum-B mirrors as a source for multiply charged ions. These ions are needed for a wide variety of applications ranging from high-Z ion injection into cyclotrons to fusion ion impurity studies to ion beam lithography and implantation. The ECR ion source has been proven the most versatile and reliable of the available sources that produce these ions. Many of these sources, though, are designed, built, and operated based on empirical knowledge acquired from past or existing machines. A few authors have attempted to understand the parametric dependences of the operation of these sources.[1,2]

The investigation presented here attempts to determine the effects of ion heating on the charge-state distributions (CSD's) of a minimum-B magnetic mirror, MIMI,[3] operated at the University of Michigan. A low-power ICR heating system has been installed to directly heat the plasma ions. The effect of this heating on ion energy distributions and ion loss processes is determined by time-of-flight spectrometer measurements made of the plasma end loss. A method is presented that separates the effect of ambipolar plasma potential spread and ion temperature. This method can be generalized to include added effects that may be important in other devices. The spectrometer is also used to measure end loss ion CSD changes with ion temperature. The ion temperature effects on the measured end loss CSD's are related to ion temperature effects on the confined CSD's through modeling of the confined plasma system and end loss. The approach uses steady-state rate equations to model the atomic processes relevant to MIMI plasmas. Charge-state-specific confinement regimes are allowed that include collisional, moderately collisional, and collisionless confinement. Experimental and computational results are shown for neon and oxygen plasmas and effects similar to those shown have been observed for argon plasmas as well.

In Sec. II we develop the method by which charge-state-specific ion temperature increases, which are directly attributed to ICR heating (ICRH), can be determined. This method is applied to the experimental results of Sec. IV, which show a resonant species temperature increase of typically 25 eV. Collisions and large resonance widths result in a "bulk" temperature increase of typically 10 eV for nonresonant species. In Sec. III the plasma model is developed that predicts changes in the CSD's as a result of the temperature increases measured using the methods of Sec. II. The experimental results, shown in Sec. IV, then employ the methods of Secs. II and III to determine ion temperature increases resulting from ICRH and relate the measured end loss CSD changes to confined CSD changes taking place at the mirror midplane. These results show the average Z of both the end loss and confined CSD's are decreased dramatically with ICRH.

Much of the work described in this paper is specifically developed for processes important to the MIMI experiment. However, the conditions under which MIMI is operated are typical of ECR ion sources and the results shown are believed to be applicable to most of these sources.

II. ICR HEATING AND ION TEMPERATURE DETERMINATION

The ICR heating system installed in MIMI uses a Nagoya III antenna and is fully described in Ref. 4. The matching and resonant circuit is shown in Fig. 1 and is used to drive peak-to-peak antenna currents of 0.2 kA at $\sim$1 MHz. These currents create the rf antenna near fields that couple to the ions. Calculations by Howard[5] have shown that cyclotron heating at low frequencies in small systems can result in a

 0899-8221/90/061195-09$02.00

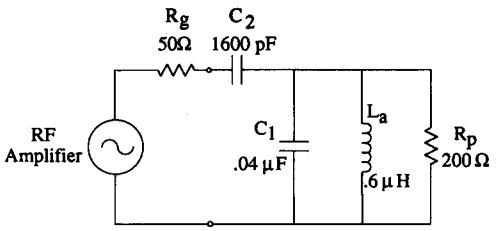

FIG. 1. Resonant and matching circuit used to drive Nagoya III ICRH antenna. Antenna losses are modeled with the parallel resistance R_p valid for $Q^2_{\text{ant}} \gg 1$. The parameters shown in the figure are chosen for a resonant frequency of $\omega_0 = 2\pi(1\text{ MHz})$. At this frequency, the wide band rf power amplifier can drive an antenna current of $I_{\text{p-p}} = 0.2$ kA.

large ion resonance widths. Assuming midplane heating and a parabolic magnetic field profile, the phase slip in radians experienced in one-half bounce period ($t_b/2$) between the left-hand circularly polarized (LCP) component of the antenna near electric field and a mirroring ion can be expressed for MIMI parameters as

$$\phi\left(\frac{t_b}{2}\right) = 340\,\frac{Q}{M^{1/2}}\left(\frac{T_{\|0}(\text{eV})}{T_{\perp 0}^{3/2}(\text{eV})}\right), \tag{1}$$

with M in atomic mass units and Q in units of proton charge. Here $T_{\|0}$ and $T_{\perp 0}$ are the midplane parallel and perpendicular ion temperatures, respectively. This is a somewhat surprising result since, for example, a singly ionized argon ion with a 5 eV parallel temperature need only be heated to 30 eV to experience resonance throughout its transit of the mirror. Even for ions where $\phi(t_b/2) \leqslant \pi/2$ does not hold true, resonance widths are still typically large. This loss of sensitivity to the location of resonance allows for ion energy absorption for a wide range of frequencies, even frequencies that place the "resonance" location outside the particle path. This near-field, large resonance width coupling, though, is generally much less efficient than coupling with a LCP traveling wave in a large system.

The effects of the ion heating are measured with a time-of-flight (TOF) spectrometer that monitors end loss ions flowing from the plasma midplane region. The spectrometer is located ~ 2 m from the plasma on a field line that maps to the magnetic axis at midplane. The method for determining ion energy distributions from TOF measurements is described in Ref. 6. Briefly, an ion packet is sampled by the TOF from the continuous plasma stream by pulsing a normally positively biased blocking electrode to ground potential. This blocking electrode is located at the entrance to the TOF spectrometer and admits ions only during the 50–300 nsec wide fast pulse. The different ion species in this ion packet are then measured using TOF techniques. If instead of pulsing the blocking electrode to ground potential, it is pulsed to an intermediate voltage V_t the current measured by the spectrometer for a given charge state is expressed as

$$I_{A_i} = \beta \int_{q_i V_t}^{\infty} f_i(E)\,dE, \tag{2}$$

where I_{A_i} = *collected current of mass species A of charge* q_i ($q_i = Z_i e$, *where* $Z_i = i$ *for* $i = 1,2,\ldots,Z_{\max}$ *is the ion charge number and e is the electron charge*) and β = *proportionality constant*. Note that the distribution functions of ions, $f_i(E)$, measured with this technique are charge-state specific.

The problem then arises of isolating the effects that determine the shape of the end loss energy distributions $f_i(E)$ measured by the TOF spectrometer and of determining how ion heating alters these measured distributions. It has been shown[6] that the shape of the end loss ion energy distributions in MIMI is determined primarily by the ambipolar plasma potential spread in the ionizing region of the plasma. Ion temperature is a second-order effect that must be separated from the effect caused by potential spread. A Monte Carlo approach is used to accomplish this. Assuming a one-dimensional Maxwellian distribution of ions of species A, charge q_i, and temperature T_{A_i}, and a plasma potential spread between $\phi_{p1} = E_1/q_i$ and $\phi_{p2} = E_2/q_i$, the two distributions that contribute to the total energy distribution measured by the TOF are

$$f_T(E) = (2/\sqrt{\pi})\left[1/(kT_{A_i})^{3/2}\right] E^{1/2} \epsilon^{-E/kT_{A_i}}, \quad 0 \leqslant E \leqslant \infty, \tag{3}$$

$$f_p(E) = 1/(E_2 - E_1), \quad E_1 \leqslant E \leqslant E_2. \tag{4}$$

The above distribution, $f_p(E)$, assumes plasma potential (ϕ_p) and ion density profiles such that an ion has an equal probability of finding itself with any given energy between E_1 and E_2. If the ion density profile is flat near the midplane, this would require that the potential profile be linear between the locations where $\phi_{p1} = E_1/q_i$ and $\phi_{p2} = E_2/q_i$. This assumption is corroborated by the close fits to experimental data shown in Sec. IV A. Small changes in the assumed shape of either the potential or density profile do not have a discernable effect on the Monte Carlo solutions for the ion energy distributions.

The two distributions described by Eqs. (3) and (4) are combined by following individual particles from the plasma and assigning them energies from each of the distributions based on Eqs. (3) and (4) and standard Monte Carlo techniques.[7] The total energy of a particle when it reaches the spectrometer will be the sum of energies gained from each of the distributions. If a sufficient number of particles are followed (~ 5000 particles/energy bin), a frequency plot of the total particle energies will approximate the combined distribution. The advantage of this method is that it is general and can be used, without added mathematical complexity, for any number of distributions that may be important in a given plasma device. It can also account for other important processes such as energy losses resulting from the scattering of ions in their flight path. Another advantage is that the method does not require analytical distributions, but can use, for example, a distribution determined from an experimentally measured plasma potential profile.

The sample results of Fig. 2 show the effect of increasing ion temperature on an ion energy distribution. For these simulations, the ambipolar potential is spread between 0 and 150 V. The ion temperature T_{A_i} of Eq. (3) is increased from (a) 10 eV to (b) 30 eV to (c) 50 eV. The data points on the plots are the Monte Carlo solutions for $f_i(E_j)$, where the E_j's are specific energy ranges along the energy axis. Since

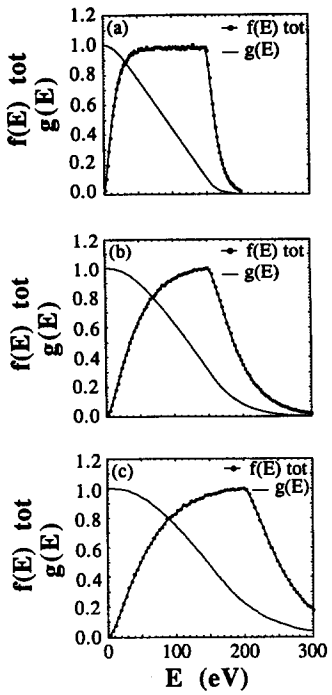

FIG. 2. Monte Carlo solutions for combined ion energy distributions for (a) $T_i = 10$ eV, 0 V$<\phi_p<$150 V; (b) $T_i = 30$ eV, 0 V$<\phi_p<$150 V; (c) $T_i = 50$ eV, 0 V$<\phi_p<$150 V. The points in the figure are the Monte Carlo solutions for the energy distributions, $f(E)$, and the solid curves are the integrated distributions, $g(E)$ [after Eq. (5)], used to fit to experimental data. Plots show the ion heating effect on the ion energy distributions.

the experimental data take the form of an integral over a given energy range, after Eq. (2), this integral of the Monte Carlo solutions is performed numerically and appears in each of the plots of Fig. 2. The integral takes the form

$$g_i(E) = \int_E^\infty f_i(E)dE . \tag{5}$$

The curves generated by Eq. (5) are the curves to which the experimental data of Sec. IV A are matched to determine ion heating effects.

Several assumptions have been made that simplify the calculations previously described. Future work might include incorporating more complex processes into the model. For example, ions are assumed to carry all their energy from the midplane region to the TOF without losing any energy, via collisions with other ions or neutrals. These collisions would have the effect of "filling in" the lower energies of the distribution and could be included using the Monte Carlo technique. Also, the form of $f_p(E)$ is chosen as an approximation that fits experimental data well. A more accurate form could involve modeling the ion density and plasma potential axial profiles and determining the resulting $f_p(E)$ in this way. This might more closely model the actual system, however, the flat-profile approximation appears to be adequate.

III. EQUILIBRIUM PLASMA MODEL AND COMPUTER SIMULATION CODE

A. Model development

Many processes occur in the plasma of an ECR ion source that affect the achievable charge-state distributions. These processes are strongly dependent on plasma parameters such as electron and ion densities and temperatures, ion mass, neutral density, average Z, etc. as well as reaction cross sections for single-impact ionization, multiple-impact ionization, charge exchange, and radiative recombination. The processes that dominate vary from source to source and depend upon individual operating parameters. An attempt is made here to model the MIMI plasma and the dominant processes that most strongly affect MIMI steady-state distributions. The modeling involved in a steady-state, equilibrium computer code used to compute ion confinement times and equilibrium charge state distributions is presented. Sample results are presented in this section and comparisons with experimental data are included in Sec. IV B.

The ion charge-state distribution (ICSD) computer code is the embodiment of a steady-state plasma model utilizing a rate equation approach to compute equilibrium charge-state distributions and charge-state-specific ion confinement times. This fluid approach is zero dimensional and uses spatially averaged quantities in its formulation. This formulation is chosen for simplicity and applicability as magnetic mirror geometry produces collisional plasmas that do not possess strong parameter gradients. The ICSD model and computer code include the following pertinent plasma processes: single-step ionization to high charge states (Auger ionization); multiple-step ionization to high charge states; transport loss; radiative recombination; and charge exchange. The steady-state rate equations, including charge quasineutrality, can be written for a specific mass species and multiply charged ion system as

$$\begin{aligned}
\frac{dn_i}{dt} = 0 = {} & n_e n_{i-1} \langle \sigma v \rangle^{\rm ms}_{i-1\to i} - n_e n_i \langle \sigma v \rangle^{\rm ms}_{i\to i+1} && \text{(multiple step)} \\
& + n_e n_0 \langle \sigma v \rangle^{\rm ss}_{o\to i} && \text{(single step)} \\
& - n_i/\tau_{i,\,\rm trans} && \text{(transport)} \\
& + n_e n_{i+1} \langle \sigma v \rangle^{\rm rr}_{i+1\to i} - n_e n_i \langle \sigma v \rangle^{\rm rr}_{i\to i-1} && \text{(radiative recombination)} \\
& + n_0 n_{i+1} \langle \sigma v \rangle^{\rm cx}_{i+1\to i} - n_0 n_i \langle \sigma v \rangle^{\rm cx}_{i\to i-1} && \text{(charge exchange)}
\end{aligned}$$

$$\text{for } 1 \leqslant i \leqslant Z_{\max} \quad \text{and} \quad \sum_{i=1}^{Z_{\max}} n_i Z_i = n_e \quad \text{(charge neutrality)} . \tag{6}$$

Note that the system described by Eqs. (6) allows for multiple impact of ions created through the single-step process. It does not include, however, further Auger ionization of ions created by either the single-step or multiple-step processes.

The above system of equations can be simplified by considering relative magnitudes of the loss terms for typical MIMI plasmas. These plasmas have been shown to produce moderately stripped ions that never become highly stripped or fully stripped ions. Therefore the above processes need only be considered for low-Z ions.

The loss processes include transport, radiative recombination, and charge exchange. The transport term in Eqs. (6) represents a dominant loss process and is therefore addressed first. The type of confinement an ion experiences is dependent on its collisionality. Ions in an ECR ion source are much more collisional than in fusion devices because of the lower ion temperatures and higher ion charges involved ($\nu_{\rm coll} \propto Z^2/T^{3/2}$). The degree of collisionality is determined by the ratio $\eta_{{\rm coll},i}$ of the bounce time of a charge-Z_i ion in the mirror to its scattering time, or equivalently, the number of scatters that an ion will experience during each bounce. Ion confinement is divided into three distinct confinement regimes dependent on the collisionality of the specific charge state in the plasma. These regimes are noncollisional confinement (Pastukhov) for which $\eta_{{\rm coll},i} \ll 1$, moderately collisional confinement (flow) for which $\eta_{{\rm coll},i} \sim 1$, and highly collisional confinement (spatial diffusion) for which $\eta_{{\rm coll},i} \gg 1$. Rognlien and Cutler[8] have shown that the flow and Pastukhov confinement times may be combined in a single expression valid for $\eta_{{\rm coll},i} \leqslant 1$. The final expressions for confinement times of mirror trapped ions in a potential well of depth ϕ and their regimes of validity may be written as follows:[8–10]

flow and Pastukhov confinement, $\eta_{{\rm coll},i} \leqslant 1$,

$$\tau_{{\rm fP},i} = RL\left(\frac{m}{kT_i}\right)^{1/2}\left[1+\tau_{ii}\frac{g(R)}{R}\frac{1}{L} \times\left(\frac{Z_i e\phi}{kT_i}\right)\left(\frac{kT_i}{m}\right)^{1/2}\right]\epsilon^{\frac{Z_i e\phi}{kT_i}}; \tag{7}$$

collisional confinement, $\eta_{{\rm coll},i} \gg 1$,

$$\tau_{{\rm coll},i} = \frac{L^2}{D_i} = \frac{L^2}{(kT_i/m)}\left(\frac{1}{\tau_{ii}}\right); \tag{8}$$

where $\tau_{{\rm fP},i}$ = confinement time valid for charge-Z_i ions in the flow–Pastukhov regime ($\eta_{{\rm coll},i} \leqslant 1$), $\tau_{{\rm coll},i}$ = confinement time valid for charge-Z_i ions in the collisional regime ($\eta_{{\rm coll},i} \gg 1$), R = mirror ratio, $g(R) = [(R+1)/R]\ln(2R+2)$, ϕ = potential dip, L = characteristic length of plasma, m = ion mass, T_i = ion temperature for charge-Z_i ion, and ϵ = base of natural logarithm.

The ion–ion scattering time, τ_{ii}, is the Spitzer 90° scattering time[11] given by the equation

$$\frac{1}{\tau_{ii}} = \sum_j \frac{1}{\tau_{ij}} = \frac{0.174 Z_i^2}{M^{1/2} T_i^{3/2}} \sum_j N_j Z_j^2 \ \mu{\rm sec}^{-1}, \tag{9}$$

where i denotes scattered particle quantities, j denotes scattering particle quantities, T_i is in electron volts, Z_i, Z_j = ion charge-state numbers, M = mass in amu, and $n_j = N_j \times 10^{11}\ {\rm cm}^{-3}$. The Coulomb logarithms have been assumed to be 10 for all species and are incorporated into the constant in Eq. (9).

It should be noted that Eq. (8) includes only effects of free diffusion. Ambipolar potential effects are not included but can be incorporated into the diffusion coefficient shown in Eq. (8). Also note that some ions in the distribution will be governed by $\tau_{{\rm fP},i}$ and some will be governed by $\tau_{{\rm coll},i}$. For collisional plasmas, confinement times vary as Z_i^2 and the higher charge states become very well confined. For moderately collisional and noncollisional plasmas, confinement time $\tau_{{\rm fP},i}$ varies as $(1+\alpha/Z_i)\exp(Z_i e\phi/kT_i)$, where α is a constant that is not a function of Z_i. Therefore if $e\phi/kT_i \ll 1$ then an increase in Z_i will result in a drop in $\tau_{{\rm fP},i}$ and if the ion temperature is not significantly greater than the potential dip, the confinement time will begin to increase again for larger Z_i. A low ion temperature will result in an increase in $\tau_{{\rm fp},i}$ with Z_i for all Z_i.

Transport losses are generally the largest of the loss processes with a typical limiting value of $n_i/\tau_{i,{\rm trans}} \sim n_i/10^{-2}\ {\rm cm}^{-3}\ {\rm sec}^{-1}$, where $\tau_{i,{\rm trans}}$ is an average ion confinement time. Radiative recombination losses can be calculated using the model of Ref. 12. Here, the radiative recombination loss for an argon plasma is considered for the worst case that would be found in a MIMI plasma. From Ref. 12,

$$\langle\sigma v\rangle^{\rm rr}_{i\to i-1} = 5.20\times 10^{-14} Z_i X_i \epsilon^{X_i}\Psi(X_i) \quad {\rm cm}^3\,{\rm sec}^{-1}, \tag{10}$$

where

$$X_i = \frac{\text{ionization potential of } i\text{th electron}}{\text{electron temperature}},$$

$$\Psi(X) = \int_x^\infty \frac{\epsilon^{-t}}{t}\,dt.$$

Assuming $Z_i = 5$ and $T_e = 5$ keV, then $\Psi(0.0182) = 3.4$. The relative losses become

$$\frac{\text{loss due to radiative recombination}}{\text{loss due to transport}} = \frac{n_e\langle\sigma v\rangle^{\rm rr}_{{\rm Ar}\,5\to 4}}{1/\tau_{i,{\rm trans}}} \sim 1.6\times 10^{-4}. \tag{11}$$

Therefore, it is evident that for charge states of interest, radiative recombination can be neglected relative to transport.

Next consider charge exchange losses for the same ions and plasma conditions. An empirical charge exchange cross section fit from Mueller and Salzborn can be expressed as[13]

$$\sigma^{\rm cx}_{i\to i-1} = A_k (Z_i)^{\alpha_k} I_p^{\beta_k}\ {\rm cm}^2, \tag{12}$$

where k = number of captured electrons = 1, $A_1 = 1.43\times 10^{-12}$, $\alpha_1 = 1.17$, $\beta_1 = -2.76$, Z_i = charge state = 5, and I_p = ionization potential = 91 eV. Using the above expression for $\sigma_{5\to 4}$, assuming 10 eV ions, and assuming a neutral background pressure of $P = 3\times 10^{-6}$ T, the relative losses for Ar^{5+} are found to be

$$\frac{\text{loss due to charge exchange}}{\text{loss due to transport}} = \frac{n_0\sigma^{\rm cs}_{{\rm Ar}\,5\to 4} v}{1/\tau_{i,{\rm trans}}} = 0.027. \tag{13}$$

Although charge exchange losses are much larger than radiative recombination losses, they are still relatively small compared to typical transport losses. Since charge exchange becomes more prevalent for higher charge states, losses for charge states much higher than five would then become an appreciable fraction of $n_i/\tau_{i,\text{trans}}$ and would then need to be included in the model. Equations (11) and (13) show that MIMI plasma losses are *transport* dominated and therefore the transport term will be the only loss term remaining in Eqs. (6).

The ionization terms of Eqs. (6) must now be considered. Following the formulation of Ref. 14, the ionization coefficients for single- and multiple-step ionization can be expressed as

$$\langle \sigma_0^i(E)v\rangle_{0\to i}^{\text{ss}} = \int_0^\infty \sigma_0^i(E)vf(E)dE = \sigma_0^{i*}\sqrt{\frac{8}{\pi m_e kT_e}}\,E_{ai}\Psi\left(\frac{E_{ai}}{kT_e}\right) \tag{14}$$

and

$$\langle \sigma_i^1(E)v\rangle_{i\to i+1}^{\text{ms}} = \int_0^\infty \sigma_i^1(E)vf(E)dE = \sigma_i^{1*}\sqrt{\frac{8}{\pi m_e kT_e}}\left(\frac{E_0}{E_{bi}}\right)^2 E_{bi}\Psi\left(\frac{E_{bi}}{kT_e}\right). \tag{15}$$

The term $\Psi(x)$ is defined in Eqs. (10). Equations (14) and (15) assume the electron distribution function $f(E)$ is Maxwellian and $kT_e \gg E_{ai}, E_{bi}$. Here E_{ai} is the threshold energy for the Auger process to remove i electrons, or equivalently, the binding energy of the subshell where one vacancy is capable of creating i vacancies via Auger transitions; E_{bi} is the threshold energy for removing the outermost electron from an i times ionized ion (i.e., the ionization potential); E_0 is the ionization potential of the neutral atom. The proportionality constants σ_o^{i*} and σ_i^{1*} are determined by experiment. These values are not well known, particularly for high charge states, and discrepancies of factors of 2 are not uncommon. Cross section data for the noble gases can be found in Refs. 15–17, from which σ_0^{i*} and σ_i^{1*} and can be computed.

B. Method of solution and sample results

All terms for the set of equations describing the buildup of a steady-state charge-state distribution in a typical MIMI plasma have been addressed. The solution of Eqs. (6) may now be approached.

Explicit forms for $\tau_{i,\text{trans}}$ ($=\tau_i$ for simplicity), the confinement time for an ion of charge Z_i, are given by Eqs. (7) and (8). There are some problems with using these expressions precisely as they appear. First, the confinement times will be discontinuous as Z_i moves from one collision regime to the next. This is a nonphysical result. Second, there is ambiguity in the constants preceding the expressions for $\tau_{\text{coll},i}$ and $\tau_{\text{fP},i}$. For example, the form of the characteristic distance L used in the expressions is uncertain. For collisional diffusion, L should be near r_p, the distance to the walls along the direction of the steepest density gradient. For collisionless loss, L should be much closer to the mirroring length since radial particle diffusion is limited by the magnetic field. Also, typically, discrepancies of factors of at least 2 are found in the constants published in the literature since these expressions are merely approximations for more exact forms. For these reasons, all dependence on n_i, T_i, R, m, Z_i, and τ_{ii} is retained in the expressions of Eqs. (7) and (8); however, the constants $RL(m/kT_i)^{1/2}$ of $\tau_{\text{fP},i}$ and $L^2(kT_i/m)$ of $\tau_{\text{coll},i}$, which are not functions of charge state, are assigned arbitrary values and computed self-consistently with Eqs. (6).

An additional requirement of continuity is imposed at the boundary of the collisional and flow–Pastukhov regimes, which relates the arbitrary constants assigned to each of the two collisional regimes mentioned above. This condition takes the form

$$1/\tau_{\text{coll},i}(Z_i = Z_c) = 1/\tau_{\text{fP},i}(Z_i = Z_c)\,, \tag{16}$$

where

$$Z_c = \tfrac{1}{2}(Z_{i\,\text{coll min}} + Z_{i\,\text{fP max}})\,, \tag{17}$$

$Z_{i\,\text{coll min}}$ = smallest Z_i for which an ion is found in the collisional regime, and $Z_{i\,\text{fP max}}$ = largest Z_i for which an ion is found in the flow–Pastukhov regime. Defined in this way, Z_c is a fictitious charge state lying halfway between the highest charge state in the flow–Pastukhov regime and the lowest charge state in the collisional regime. The regime for each charge state is assigned on the following basis:

$$\eta_{\text{coll},i} = t_{bi}/\tau_{ii} \leqslant 10 \Rightarrow \text{flow–Pastukhov}, \tag{18}$$

$$\eta_{\text{coll},i} = t_{bi}/\tau_{ii} > 10 \Rightarrow \text{collisional}, \tag{19}$$

where τ_{ii} is given in Eq. (9) and

$$t_{bi} = \text{ion bounce time} = \pi L_m/v_{10}\,, \tag{20}$$

assuming a parabolic magnetic field profile $B = B_0(1 + z^2/L_m^2)$.

With the above definitions, confinement times for the entire distribution may be derived:

$$1/\tau_i = \alpha_0 X_i\,, \tag{21}$$

where

$$X_i = \begin{cases} \tau_{ii}(Z_i)\,, & Z_i > Z_c\,, \\ \tau_{ii}(Z_c)[h(Z_c)/h(Z_i)]\epsilon^{(Z_c - Z_i)(e\phi/kT_i)}, & Z_i < Z_c, \end{cases}$$

with

$$h(Z_i) = 1 + \tau_{ii}(Z_i)\frac{g(R)}{R}\frac{1}{L}\left(\frac{Z_i e\phi}{kT_i}\right)\left(\frac{kT_i}{m}\right)^{1/2}.$$

The number of unknowns for the system of $(Z_{\max}+1)$ coupled equations, Eqs. (6), is now reduced to $(Z_{\max}+1)$. The unknowns are $\{n_i\}$ for $1 \leqslant i \leqslant Z_{\max}$ and α_0. The symbol $\{\ \}$ represents a vector quantity. The form of the confinement times precludes an analytical solution since τ_i is a complicated function of $\{n_i\}$ and Z_i. It can be shown, though, that the system of equations is unconditionally convergent for all physical values of densities, temperatures, masses, etc. The system is solved using the computational iterative scheme described by the following: (1) Input values for $\{\sigma_0^{i*}\}$, $\{\sigma_i^{1*}\}$, $\{E_{ai}\}$, $\{E_{bi}\}$, $Z_{\max}$, M, L_m, R, ϕ, T_e, T_i, n_e, and n_0; (2) compute $\langle\sigma v\rangle$'s for input T_e (separate code); (3) assign

an initial estimate for $\{n_i\}$ for $1 \leqslant i \leqslant Z_{max}$. Since the system is so strongly convergent, this estimate does not change for varying input parameters; (4) assign confinement regimes for each charge state based on $\{n_i\}$; (5) solve the system of equations for α_0 given $\{n_i\}$ and Z_c; (6) compute a new $\{n_i\}$ given the new α_0 and Z_c; (7) compute a new Z_c for $\{n_i\}$, α_0, (8) If $Z_{c\,new} \neq Z_{c\,old}$ then repeat steps (4)–(8) until Z_c does not change. When Z_c remains the same for two consecutive iterations, the solutions for $\{n_i\}$, α_0, and Z_c are self-consistent; (9) compute $\{\tau_i\} = f(\{n_i\},\alpha_0,Z_c)$; and (10) output results: $\{n_i\},\{\tau_i\}$.

A set of sample results is shown in Fig. 3. Figure 3(a) shows the computed normalized ion densities as a function of charge state for several neutral background densities. As the neutral background pressure is decreased, a gradual shift to higher charge states occurs. This is a result of large $n_0\langle\sigma v\rangle_{0\to1}$ reaction rates for large neutral pressures. If n_0 is large, the reaction rate, $n_0\langle\sigma v\rangle_{0\to1}$, will dominate and a large Ar^{1+} population will develop. As n_0 is decreased, reaction rates of other processes become comparable to the $n_0\langle\sigma v\rangle_{0\to1}$, rate, and, since charge neutrality must be maintained, higher charge states gradually become populated.

The computed confinement times for case 3 of Fig. 3(a) (lowest n_0 and highest $\langle Z\rangle$) are shown in Fig. 3(b). For this case, only the first two charge states in the distribution lie in the flow–Pastukhov regime. All charge states with $Z_i \geqslant 3$ are collisionally confined. The curves plotted are computed confinement times assuming either an entirely collisional or an entirely collisionless plasma. The ICSD solution for the confinement times are plotted as data points and show a smooth transition between the two regimes at $Z_i = Z_c = 2.5$.

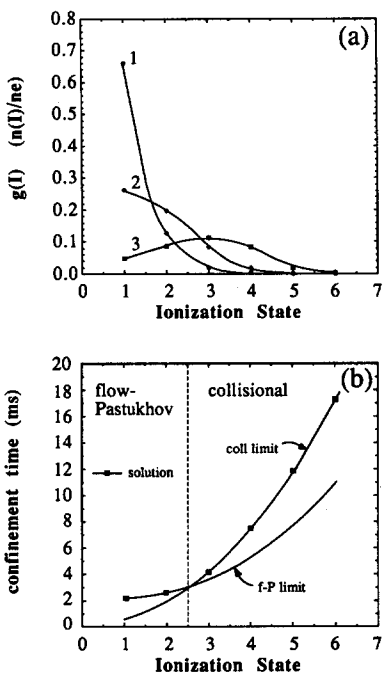

FIG. 3. Sample solutions from ICSD simulations for an argon plasma. The plasma parameters are $n_e = 2\times10^{11}$ cm^{-3}, $T_e = 5$ keV, $\phi = 2$ V, $T_i = 5$ eV. (a) Normalized ion densities for case (1), $n_0 = 1\times10^{11}$ cm^{-3}; case (2), $n_0 = 0.1\times10^{11}$ cm^{-3}; and case (3) $n_0 = 0.01\times10^{11}$ cm^{-3}. (b) Computed confinement times for case (3). Ions with $Z_i = 1,2$, lie in the flow–Pastukhov confinement regime, governed by Eq. (7), and ions with $Z_i > 3$ lie in the collisional confinement regime, governed by Eq. (8). The curves show the smooth transition of the solution between the two confinement regimes at $Z_i = Z_c = 2.5$.

Figure 3 is a sample result from the ICSD code. Modeling of the actual system using this code and comparison to experimental data will be presented in Sec. IV B.

C. ICSD model limitations

Several simplifying assumptions have been made in the ICSD model that may or may not be important in plasma devices other than MIMI. These can be incorporated in revisions of the model and are mentioned here for completeness. Radiative recombination has been shown to be negligible relative to transport. Radiative recombination rates are so small that they may be neglected for all but the highest charge states. Charge exchange losses become comparable to transport losses for either high neutral pressures or high-Z ions. For systems where medium-to-high-Z ions are produced, charge exchange becomes an important process. The form of the diffusion coefficient D_i of Eq. (8) may be altered to include ambipolar diffusion effects. This is not expected to change D_i by more than a factor of 2–3. Last, the ICSD model assumes a one-temperature electron population. Measurements indicate that the system is more closely modeled by two electron populations characterized by "hot" and "cold" electron temperatures. Cold electrons are not expected to contribute significantly to ionization but may be important in charge exchange and radiative recombination (shown to be negligible for MIMI). Therefore a model allowing for two electron populations may more closely model an actual ECR ion source system.

IV. ICR HEATING EXPERIMENTAL RESULTS

A. Ion energy distribution measurements

The time-of-flight spectrometer is capable of measuring ion energy distributions as described in Sec. II. The data take the form described by Eq. (2) and are fitted to the output of the Monte Carlo simulations similar to those shown in Fig. 2. These fits determine the individual contributions of ion temperature and ambipolar plasma potential spread to the total measured integrated distribution of Eq. (2). In this way, ion temperature changes with ICRH can be deduced.

Figure 4 illustrates the effect of ion cyclotron heating on the measured distributions of O^{2+}. The heating frequency chosen is that which corresponds to the cyclotron frequency of the third charge state of oxygen at $B = 2700$ G, the magnetic field at the ECR resonance zones. It is assumed that the energy distribution from the plasma potential spread has the form of Eq. (4) with $E_1 = 0$. The effect of the ICRH is determined from plots, such as those of Fig. 2, as follows. End loss ion charge-state distributions are measured with the TOF spectrometer with and without ICRH as functions of gating-grid voltage. This will generate the data points shown in Fig. 4. For the case without ICRH, the midplane ion temperature is assumed small (10 eV) relative to the energy gained from the ambipolar potential. A best fit of the Monte Carlo code output, $g_i(E)$, determines the midplane plasma potential spread assuming a flat ion density profile near midplane.

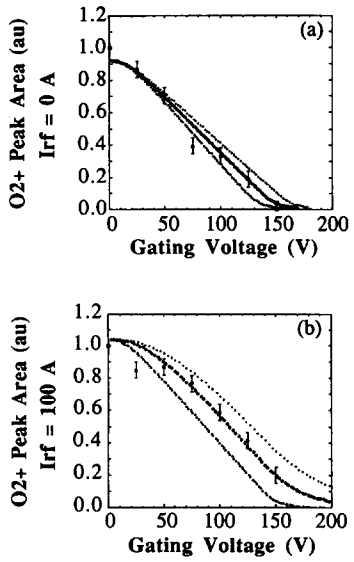

FIG. 4. Determination of plasma potential spread and ICRH ion temperature increase of O^{2+} using a Monte Carlo fit to TOF data. (a) O^{2+} peak area versus gating-grid voltage for $I_{rf} = 0$ A and Monte Carlo fits for $T_i = 10$ eV and $0\ V < \phi_p < 120$ V, $0\ V < \phi_p < 135$ V, $0\ V < \phi_p < 150$ V. The fits show a sensitivity of < 15 eV. (b) O^{2+} peak area versus gating-grid voltage for $I_{rf} = 100$ A and Monte Carlo fits for $0\ V < \phi_p < 135$ V and $T_i = 10$ eV, $T_i = 25$ eV, $T_i = 40$ eV. This fit assumes no change in the plasma density or ambipolar potential profiles with ICRH. The figure shows an ion temperature increase of ~ 15 eV with ICRH. The peak area is the integrated area under each ion species peak in the TOF output and is proportional to the collected current for that species.

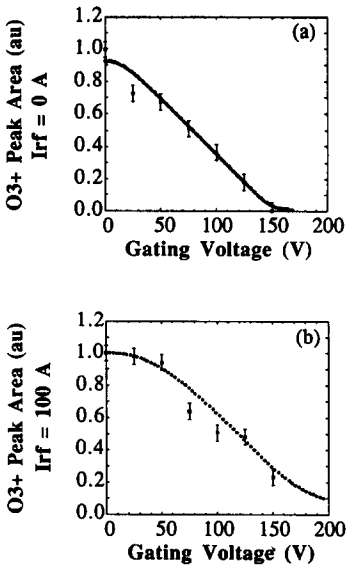

FIG. 5. Determination of plasma potential spread and ICRH ion temperature increase of O^{3+} using a Monte Carlo fit to TOF data. (a) O^{3+} peak area versus gating-grid voltage for $I_{rf} = 0$ A and Monte Carlo fit for $T_i = 10$ eV and $0\ V < \phi_p < 135$ V. (b) O^{3+} peak area versus gating-grid voltage for $I_{rf} = 100$ A and Monte Carlo fit for $0\ V < \phi_p < 135$ V and $T_i = 40$ eV. The resonant O^{3+} ions have gained 15 eV more than the nonresonant O^{2+} ions of Fig. 4.

This is illustrated in Fig. 4(a). This spread is assumed to remain constant with the application of ICRH. This assumption is corroborated by the observation of little or no change in the plasma conditions when ICRH is applied. Therefore, the change in the shape of the peak area versus V_{pulse} curve is assumed to be a direct result of increased ion temperature. The best fit to these data then determines the increase in T_i with ICRH. Figure 4(a) shows three fits to the data for $0\ V < \phi_p < 120$ V, $0\ V < \phi_p < 135$ V, and $0\ V < \phi_p < 150$ V. The best fit shows that this method has a resolution of < 15 eV for determining the plasma potential spread. Assuming the best fit of $E_2 = 135$ V, T_i is increased in Fig. 4(b) until a good match to the data is achieved. Again, three cases are shown for $T_i = 10$ eV, $T_i = 25$ eV, and $T_i = 40$ eV. Clearly, the $T_i = 25$ eV case is the best fit, which shows a 15 eV increase in the O^{2+} ion temperature with ICRH. Figure 4(b) also shows the sensitivity of this measurement to be ~ 5 eV.

Figure 5 shows the same fits to the O^{3+} ion for the same shots of Fig. 4. The fit for the case of $I_{rf} = 0$ A must be the same as for the O^{2+} ion since the plasma potential profile affects both distributions in the same manner. They are indeed identical. The fit for the case of $I_{rf} = 100$ A, though, shows an ion temperature of 40 eV. This is 15 eV higher than the O^{2+} case. This is consistent with the concept of heating the 3+ charge state and transferring, through collisions, the absorbed energy to the remainder of the distribution. Calculations show ion energy exchange times small compared to typical confinement times. Also, the possibility of direct heating of nearby charge states exists as the resonance zones of high charge states often overlap. Similar ion heating effects have been observed in both neon and argon.

B. Ion charge-state distribution measurements

Ion cyclotron resonance heating has been implemented in MIMI to effect direct energy transfer to the plasma ions. This section deals with the effect of this energy transfer on the steady-state ion charge-state distributions. Measured effects are reported for neon, as are correlations with the modeling code ICSD discussed in Sec. III. Confinement-time sensitivity to ion temperature and its resultant effect on the TOF signal is accounted for in comparing the measured effect with the model. A "mapping" is performed to relate the measured end loss charge-state distribution changes to the changes occurring in the confined midplane plasma.

Data for the measured ion signals of neon as a function of antenna rf current are shown in Fig. 6. A scattering of data points taken for identical plasma conditions is used instead of error bars to indicate confidence in the measured quantities. The data are normalized to negate the spectrometer's sensitivity to mass-to-charge ratio. The most obvious effect of ion heating is the precipitous decrease, with rf current, in the current densities of the highest charge states. The current densities of the lowest charge states remain constant or even increase with the highest rf currents. For neon, the overall effect of the ion heating is therefore to decrease the average Z of the extracted ions.

The results of Sec. V A show that with the rf currents of Fig. 6, ion temperatures are markedly affected. This increase in ion temperature will affect the ion confinement times in

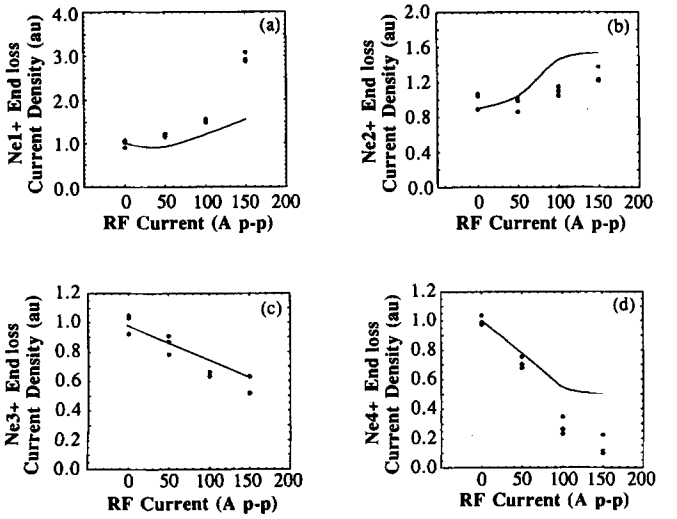

FIG. 6. Measured (data points) and computed (curves) neon ion end loss charge state distribution changes with ion temperature. Values are plotted as a function of antenna rf current that is related to ion temperature after Eq. (24). For this simulation, ion temperature is assumed to vary from $T_i = 5$ eV at $I_{rf} = 0$ A to $T_i = 30$ eV at $I_{rf} = 150$ A, and $\phi = 15$ eV. The ICSD code input has been corrected for slight measured changes in electron density with antenna current. Both modeling and measurement show a shift to lower average Z with increased ion temperature.

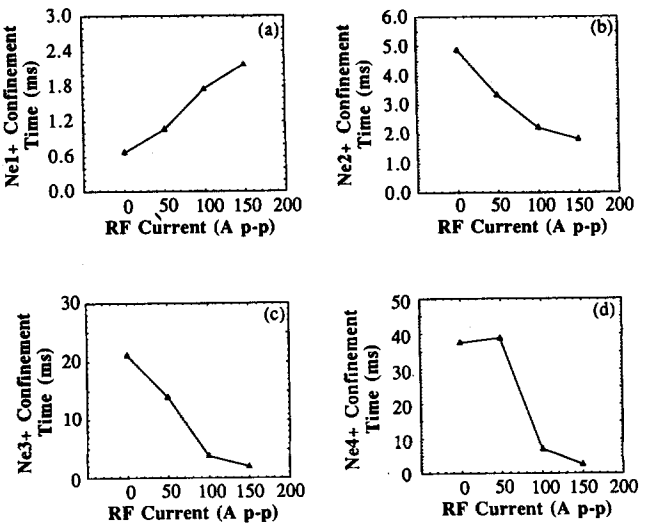

FIG. 7. Computed neon confinement-time changes with ion temperature for conditions of Fig. 6. Values are plotted as a function of antenna rf current, which is related to ion temperature after Eq. (24). Shows decreased confinement times for high charge states with ion temperature.

the plasma after Eqs. (7) and (8). These equations show for flow–Pastukhov confinement, $\eta_{\text{coll},i} \leqslant 1$,

$$\tau_{\text{fP},i} \propto (1 + \beta T_i)\epsilon^{Z_i e\phi/kT_i}; \tag{22}$$

for collisional confinement, $\eta_{\text{coll},i} \gg 1$,

$$\tau_{\text{coll},i} \propto 1/T_i^{3/2}; \tag{23}$$

where T_i = ion temperature, ϕ = potential dip, and β = const—not a function of T_i. This ion confinement change with temperature can be accounted for by the ICSD code. By matching the predicted loss rates from the code to the measured loss rates and then imposing the conditions required for this match on the system, the *confined* densities of each of the charge states can be computed. The ICSD code computes confinement times and densities of each of the charge states present in the mirror. The loss rates of a given charge state Z_i vary as n_i/τ_i. Since $\tau_i \propto f(T_i)$, the change in τ_i with rf heating must be included in the match to the measured data. The ion temperature is assumed to vary with the rf antenna current as

$$T_i = T_0 + \gamma I_{\text{rf}}^2, \tag{24}$$

where γ = *proportionality constant* (eV/A^2). For each case, the ion temperature increase, γI_{rf}^2, with rf heating is held consistent with the temperature increase found using the Monte Carlo fits to neon time-of-flight plots similar to the plots of Figs. 4 and 5. The initial ion temperature T_0, and ϕ, the confining potential dip, are adjusted to yield the best fit to the data. These best fit values, though, are consistent with values expected from other independent measurements.

The best ICSD loss-rate fit is shown as the curves in Fig. 6. The main parameters are given in the figure. The electron density is monitored during the runs of Fig. 6 and the code inputs are corrected for slightly varying densities. For these runs, the neutral background is considered to be 99% ionized. The code predicts the general measured trends of each of the charge states with increasing ion temperature. Again the computed signal of the high-charge-state end loss is seen to decrease with temperature, though not as quickly as measured by the TOF spectrometer. Both the Ne^{1+} and Ne^{2+} end loss rates are predicted to increase with ion temperature, as they must to remain charge neutral. The spectrometer effectively measures n_i/τ_i so that if confinement times vary strongly with ion temperature, the measured signals can be markedly affected even if the confined density remains relatively unchanged. Figure 7 shows that this is indeed the case. The confinement time for singly ionized neon is seen to rise with ion temperature, consistent with the flow confinement mode of Eq. (22). As the ion charge increases, the confinement times are seen to fall quickly with temperature. This is a result of the fact that the ions become more collisional with increased Z_i and move into the collisional confinement regime where $\tau_i \propto 1/T_i^{3/2}$. Also, for those ions that do remain flow confined, with increasing Z_i the magnitude of the exp $(Z_i e\phi/kT_i)$ term of Eq. (22) becomes a strong function of T_i, decreasing rapidly with increasing T_i. This rapid decrease in confinement time has the effect of increasing the measured signals above that which would be expected from mere confined densities alone. Alternatively, the increasing confinement time of the single ionized state of Fig. 7, decreases the measured signal of Ne^{1+}.

The conditions are now determined for the best fit between the measured and computed end loss current densities. The *confined* charge-state distributions may now be computed. Results for these confined densities for the conditions of Fig. 6 are shown in Fig. 8 for the first four charge states of neon. As with the end loss densities, the confined densities of the high charge states decrease rapidly with ion temperature. This is a consequence of the rapid decrease in confinement with temperature prescribed by Eqs. (22) and

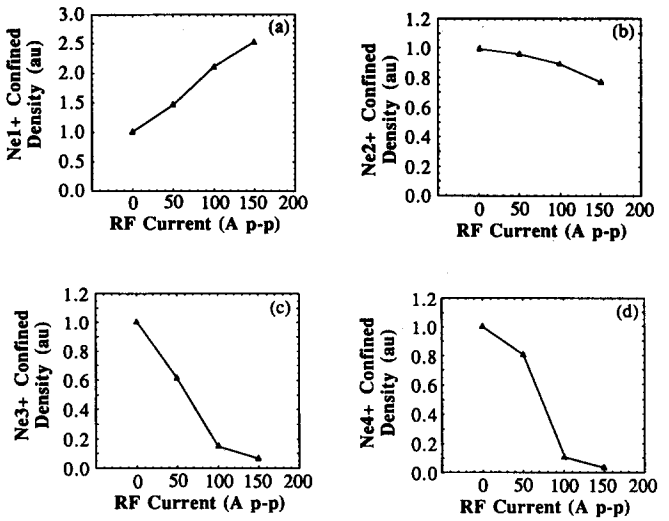

FIG. 8. Computed neon confined density changes with ion temperature for conditions of Fig. 6. Values are plotted as a function of antenna rf current, which is related to ion temperature after Eq. (24). As in the case of end loss densities, confined densities of high charge states decrease rapidly with ion temperature.

(23) and shown in Fig. 7. Charge neutrality must still be maintained, though, which accounts for the increase in the confined densities of the low charge states whose confinement is not negatively affected by temperature changes.

With increased ICRH, a marked shift to lower charge states occurs as a result of the decreasing confinement times of high charge states with temperature. At large rf powers, results of both measurement and modeling show almost complete loss of all charge states above the first three.

V. DISCUSSION

Low-power ICRH effects in the ECR-heated ion source, MIMI, have been described. Ion energy distribution measurements determine typical resonant species temperature increases to be 30 eV and nonresonant species temperature increases to be 15 eV. Ion temperatures with no direct ion heating are typically below 10 eV. A method has been presented that separates the effect of ion temperature and plasma potential spread on the ion end loss energy distributions. This method is used to determine the ion heating effects. The measured ion temperature increases and measured ion charge state distributions are used in a steady-state, equilibrium code to determine the ion heating effects on the confined ion charge-state distributions. This code was developed to model atomic processes relevant to MIMI and similar ECR ion sources. It allows for single-step and multiple-step ionization to high charge states. It also allows for collisional confinement, moderately collisional confinement and collisionless confinement specific to each charge state in the distribution. Results show that for many operating conditions most of the charge-state distribution is governed by collisional confinement. The code allows for a smooth transition between the confinement regimes. Both measurement and modeling results show a rapid decrease in the density of high charge-state ions with ion temperature. This is a result of loss of high-Z ion confinement with large T_i. The densities of the lowest charge-state ions increase with temperature causing an overall shift to lower average Z.

ACKNOWLEDGMENTS

The authors would like to thank J. Booske for use of his rf equipment, without which much of the experimental work presented here would not have been possible.

This work is partially supported by the National Science Foundation. D. R. Whaley has been partially supported by the U. S. Department of Energy Magnetic Fusion Energy Technology Fellowship program.

[1] J. Booske, F. Aldabe, R. Ellis, and W. Getty, J. Appl. Phys. **64**, 1055 (1988), and references contained therein.

[2] See National Technical Information Service Document No. DE 84000517 (*Calculation of Ion Charge-State Distributions in ECR Ion Sources*, UCRL-53391, by H. West, Jr., Lawrence Livermore National Laboratory, 1982). Copies may be ordered from the National Technical Information Service, Springfield, Virginia 22161. The price is $15.95 plus a $3.00 handling fee. All orders must be prepaid.

[3] J. Booske, W. Getty, R. Gilgenbach, and R. Jong, Phys. Fluids **28**, 3116 (1985).

[4] D. R. Whaley, Ph.D. dissertation, University of Michigan, 1989.

[5] J. Howard, Plasma Phys. **23**, 597 (1981).

[6] D. Whaley, T. Goodman, and W. Getty, Rev. Sci. Instrum. **60**, 358 (1989).

[7] W. Selph and C. Garrett, in *Reactor Shielding for Nuclear Engineers*, edited by N. M. Schaeffer (U. S. Atomic Energy Commission, Oak Ridge, TN 1973), p. 207.

[8] T. Rognlien and T. Cutler, Nucl. Fusion **20**, 1003 (1980).

[9] V. Pastukhov, Nucl. Fusion **14**, 3 (1974).

[10] D. Smith and C. Petty, Bull. Am. Phys. Soc. **31**, 1511 (1986).

[11] L. Spitzer, Jr., *Physics of Fully Ionized Gases* (Interscience, New York, 1962).

[12] D. Post, R. Jensen, C. Tarter, W. Grasberger, and W. Lokke, Atom. Data Nucl. Data Tables **20**, 397 (1977).

[13] A. Mueller and E. Salzborn, Phys. Lett. A **62**, 391 (1977).

[14] G. Fuchs, IEEE Trans. Nucl. Sci. **NS-19**, 160 (1972).

[15] B. Schram, A. Boerboom, and J. Kistemacker, Physica **32**, 185 (1966).

[16] B. Schram, Physica **32**, 197 (1966).

[17] M. Van der Weil, T. El-Sherbini, and L. Vriens, Physica **42**, 411 (1969).